Intermetallics 173 (2024) 108439

Contents lists available at ScienceDirect

Intermetallics

journal homepage: www.elsevier.com/locate/intermet

Gas tungsten arc welding of a multiphase $CoCu_xFeMnNi$ (x=20,30) high entropy alloy system: Microstructural differences and their consequences on mechanical performance

J.G. Lopes [a,*], M. Varela [a], S.H. Shim [c], N. Schell [d], E. Maawad [d], S.I. Hong [c], A.C. Baptista [b], J. P. Oliveira [b,**]

[a] UNIDEMI, Department of Mechanical and Industrial Engineering, NOVA School of Science and Technology, Universidade NOVA de Lisboa, Caparica 2829-516, Portugal
[b] CENIMAT/I3N, Department of Materials Science, NOVA School of Science and Technology, Universidade NOVA de Lisboa, 2829-516 Caparica, Portugal
[c] Department of Materials Science and Engineering, Chungnam National University, Daejeon, 34134, South Korea
[d] Institute of Materials Physics, Helmholtz-Zentrum Hereon, Max-Planck-Str. 1, 21502 Geesthacht, Germany

ARTICLE INFO

Keywords:
High entropy alloys
CoCuFeMnNi
Gas tungsten arc welding
Synchrotron X-ray diffraction
Thermodynamic calculations
Mechanical testing

ABSTRACT

With the current advancements in materials science, the development of high entropy alloys (HEAs) is progressively increasing. Hence, research on their processability is essential to make them competitive alternatives to common engineering alloys that are widely used in structural applications. One manufacturing technique commonly employed in this sector is gas tungsten arc welding (GTAW). This technique allows to obtain single monolithic parts from separate components, often at the cost of local microstructural and mechanical properties variation across the joint. As such, GTAW processing is capable of supplying relevant knowledge regarding the feasibility of joining new materials and their potential industry uptake. In this study, we present a comparative analysis on the use of GTAW on two distinct multiphase high entropy alloys: $CoCu_{20}FeMnNi$ and the $CoCu_{30}$-FeMnNi. Firstly, microstructural observations coupled with CalPhaD-based calculations and synchrotron X-ray diffraction analysis, allowed to delve, and compare, the microstructural evolution across both welds. It was possible to observe the dual phase nature of the microstructure throughout the welded joint alongside the nucleation of a B2 BCC phase in the heat affected zone (HAZ) of both HEAs. Considering the mechanical properties of the welded materials, results evidenced a poorer, yet still acceptable mechanical performance. The observed decrease in mechanical strength is attributed to the residual stress conditions and large grain size that developed owing to the process thermal cycle, which contrasted deeply with the microstructure of each base material.

1. Introduction

Conventionally, the most common alloys utilized nowadays are based on a principal element with small additions of other elements to improve their properties. In 2004, however, the inception of what would be called high entropy alloys (HEAs) took place, where the restrictions related to the amount of each element in a metal were widened [1–4]. This granted a vast unexplored compositional space to become possible allowing novel and unimaginable materials to be developed.

Although capable of showcasing outstanding properties, the processability of HEAs and the effect of such processes on their properties and performance still needs to be researched. This is especially important when a new promising HEA composition is developed. Concerning the topic of processing, gas tungsten arc welding (GTAW) is a widely used technique to achieve strong and permanent joints between independent components. Nevertheless, given the high temperatures generated to achieve joining, inevitably localized alterations to the microstructure and mechanical behavior are prone to occur. Such alterations can appear in the form residual stress distribution and, in cases, where different phases are expected to occur, phase fraction, alongside the nucleation of unexpected intermetallic compounds [5–7]. Moreover, the weld thermal cycle will also impact the size and morphology of the

* Corresponding author.
** Corresponding author.
E-mail addresses: jcg.lopes@campus.fct.unl.pt (J.G. Lopes), jp.oliveira@fct.unl.pt (J.P. Oliveira).

https://doi.org/10.1016/j.intermet.2024.108439
Received 23 June 2024; Received in revised form 26 July 2024; Accepted 29 July 2024
Available online 31 July 2024

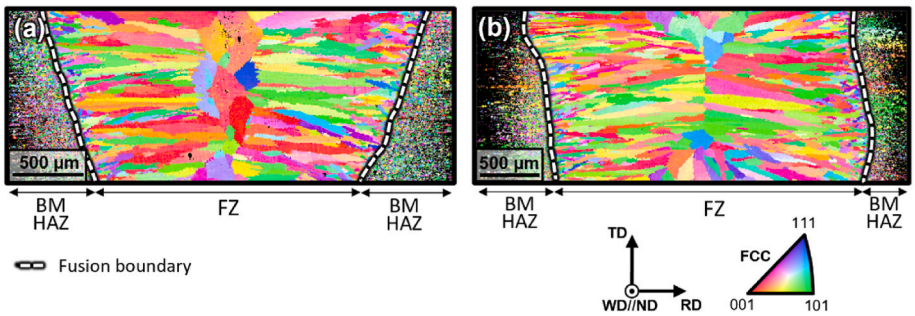

Fig. 1. Representative electron backscatter IPF macroscopic images of the welded joints of: (a) $CoCu_{20}FeMnNi$; (b) $CoCu_{30}FeMnNi$.

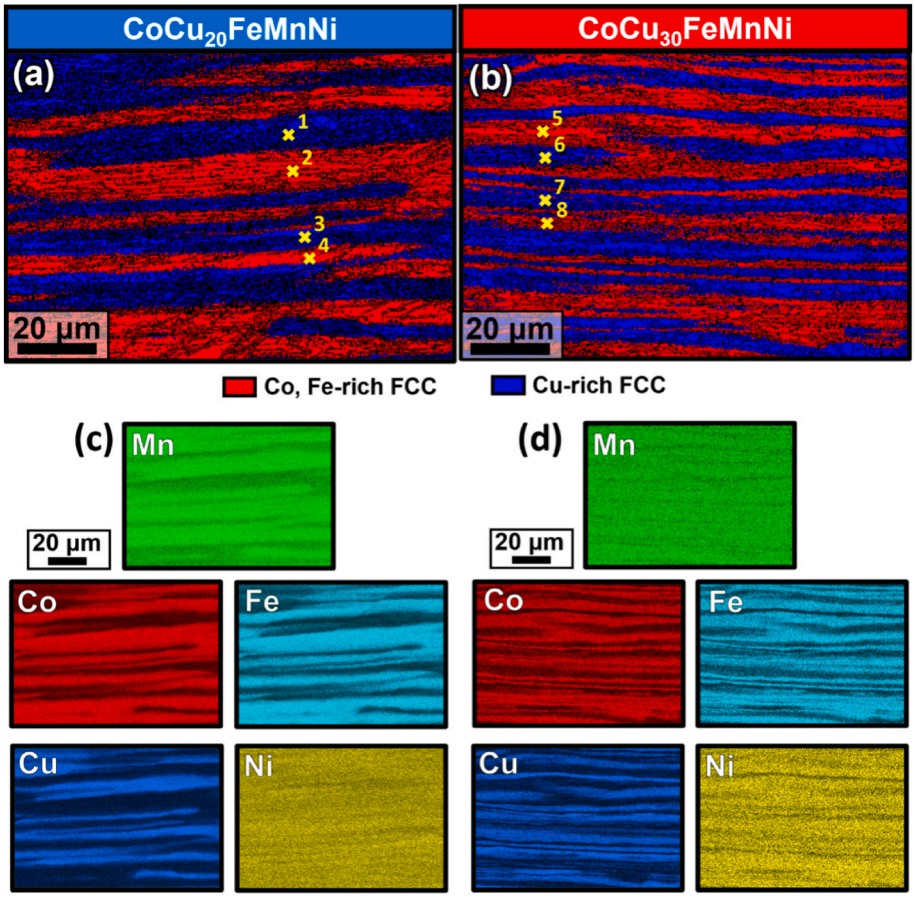

Fig. 2. EBSD phase maps highlighting the initial condition of the (a) $CoCu_{20}FeMnNi$ and (b) $CoCu_{30}FeMnNi$ HEAs, alongside with the corresponding elemental distribution in (c) for the $CoCu_{20}FeMnNi$ and (d) for the $CoCu_{30}FeMnNi$ BMs.

Table 1
– Elemental distribution of both HEAs of the EDS points marked in Fig. 2 a) and b) (The predominant elements on each point are in bold, highlighting which phase it corresponds to).

$CoCu_{20}FeMnNi$					
Point	Co	Cu	Fe	Mn	Ni
1	9	**42.4**	7.3	22.9	18.4
2	**26.2**	10.1	**28.5**	15.9	19.3
3	8.4	**40.7**	6.9	26.5	17.5
4	**24.4**	11.8	**26.1**	17.9	19.8
$CoCu_{30}FeMnNi$					
5	10.4	**46.5**	9.1	18.5	15.5
6	**24.6**	14.3	**26.1**	16.1	18.9
7	10.6	**45.4**	10.5	18.2	15.3
8	**21.9**	17.7	**23.8**	17.1	19.5

grain structure, which is conditioned as well by the previous base material thermomechanical processing,

In this work, welding of two HEAs from the CoCuFeMnNi system is performed. The difference between the two alloys mainly resides in the amount of Cu in their composition. In one hand, we have an equiatomic $CoCu_{20}FeMnNi$ alloy, while in the other hand exists a non-equiatomic $CoCu_{30}FeMnNi$ HEA. In both cases, these HEAs are characterized by possessing at least two phases in their microstructure [8]. As such, the available literature indicates that the main drive for research on these two HEAs is their mechanical performance, with the equiatomic CoCuFeMnNi being able to reach up to 2 GPa, at the cost of ductility [9–11]. Furthermore, also worthy of mention are other studies, where focus is given to the driving forces responsible for the formation of characteristic dual phase microstructure and the subsequent correlation with mechanical performance [12–14]. Nevertheless, although these topics have

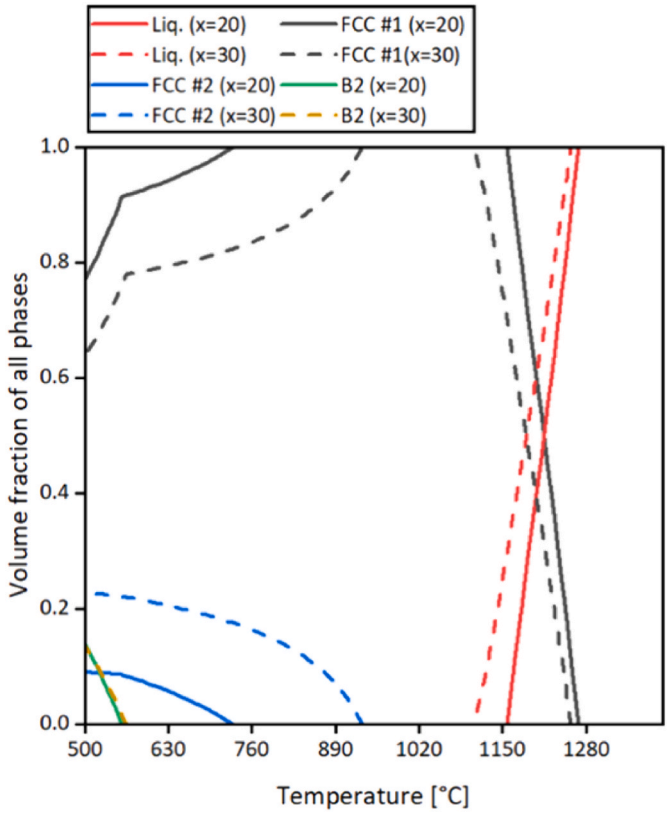

Fig. 3. One axis equilibrium performed to evaluate the phase formation in equilibrium conditions. The calculations were computed using TCHEA5 databases.

been addressed, the processability, namely the weldability, and the relation between the initial condition of the materials and their post-processed state must also be analyzed. Currently, only the weldability of the equiatomic CoCuFeMnNi HEA was assessed using laser welding [15] and transient liquid phase bonding [16]. In both cases, it was demonstrated the practicality of these alloys for engineering purposes. However, the change in composition, especially the higher fraction of Cu can potentially lead to defects associated to liquation cracking. Moreover, the use of low-cost arc-based welding processing was not yet attempted for these alloys, showing a gap in the existing body of knowledge associated to the welding of HEAs at large.

With this in mind, in this study we seek to compare the differences between the two mentioned HEAs, arising from GTAW. Such is achieved by means of optical and electron microscopy, thermodynamic analysis, and synchrotron X-ray diffraction on the full extension of the welded joints. Furthermore, tensile testing and microhardness mapping allowed us to correlate the microstructural features with the obtained mechanical behavior of the welds.

2. Materials and methods

In this study, GTAW of two multiphase HEAs belonging to the $CoCu_xFeMnNi$ system, with a varying Cu content (x = 20 and 30), were evaluated. Both equiatomic and non-equiatomic HEA ingots were cast by employing vacuum induction melting using the mixture of raw materials with high purity (above 99.9 %). After homogenizing at 1000 °C for 24 h, the rod-type specimen, with a diameter and length of ≈11.5 mm and ≈110 mm, respectively, was cut by electrical-discharge machining. The machined rod-shaped samples were then rod-rolled to a diameter of ≈2 mm at room temperature.

Prior to welding, the samples were cleaned using acetone. The optimized welding parameters were conducted using a single spot weld, where a welding current of 46 A was applied during 0.4 s. The welding procedure was performed using a CITOTIG 2200 FORCE equipment. Additionally, a constant flow of pure Argon (99,999 %) was maintained to avoid oxidation and protect the joints.

For microscopical analysis, standard metallographic techniques were followed, where optical micrographs were obtained after etching the samples with a Nital 5 % solution, using a Leica DMI5000 M inverted optical microscope. Advanced characterization was performed on a TESCAN-CLARA, ZEISS-Merlin, field-emission scanning electron microscope (SEM) using electron backscattered diffraction (EBSD) and energy dispersive X-ray spectroscopy (EDS) detectors, to acquire inverse pole figure (IPF) and phase distribution and composition maps. To further inspect the microstructural condition of the welded joints, consecutive synchrotron X-ray diffraction (SXRD) scans were performed throughout the full extent of the samples. Analysis of the SXRD data was achieved using DIOPTAS [17] and GSAS II [18] combined with single peak analysis using in-house developed python scripts.

The phase distribution and solidification paths attained during the cooling of the molten pool were assessed via CalPhaD analysis, using Thermo-Calc [19] (TCHEA 5 database) and correlated with the obtained microstructure.

Electrochemical characterization was conducted in a standard three-electrode setup using a potentiostat/galvanostat Interface 1010 from Gamry Instruments. For such, samples from the obtained welded joints in both HEAs served as the working electrode, while a platinum wire acted as the counter electrode and an Ag/AgCl reference electrode was utilized as the reference electrode. Firstly, each sample was immersed in a 3.5 wt% NaCl electrolyte solution for 2 h to establish a steady state of the open circuit potential (OCP). Then, potentiodynamic polarization measurements were conducted at a scan rate of 1 mV/s, followed by electrochemical impedance spectroscopy (EIS) measurements performed across a frequency range of 1 Hz–100 kHz.

Mechanical characterization was performed using tensile testing combined with digital image correlation (DIC). An Autograph Shimadzu AG50kNG tensile machine equipped with a 50 kN load cell and operating at a 0.01 mm/s cross-head displacement speed was used. Analysis of the post-fracture surfaces was performed on a Hitachi SU8000 SEM. Furthermore, microhardness mapping was conducted on a Mitutoyo Micro Hardness Testing Machine HM-112 with a 0.5 Kg load, applied during 10 s. A distance of 0.15 mm was kept between consecutive indentations in both longitudinal and transverse directions.

3. Results and discussion

3.1. Microstructural characterization of the joints and CalPhaD analysis

After GTAW, welded joints with full penetration without any visible defects were obtained. As such, standard metallographic preparation techniques were employed on the $CoCu_xFeMnNi$ (x = 20 or 30 at. %) welded samples. Fig. 1 depicts representative electron backscatter diffraction inverse pole images (EBSD IPF) of the resulting joints.

At a first glance it is possible to observe that in both cases large and highly aligned columnar grains grew from the base material (BM) towards the center of the fusion zone (FZ), differing massively from the highly deformed microstructure that composes the BM. In fact, the microstructure of the BM corresponds to the black (non-indexed) regions of the EBSD IPF maps, where the highly distorted microstructure prevents proper indexation of the Kikuchi patterns. Nevertheless, the impact of the heat input on the heat affected zone (HAZ), formed between the non-affected BM and the FZ, is clear due to the existence of a refined grain structure with an average grain size of 4.56 ± 0.61 μm and 4.54 ± 1.26 μm, for the $CoCu_xFeMnNi$ alloys with x = 20 or 30, respectively. It should also be noted that at the fusion boundary there is the development of a refined grain structure, due to the high cooling rates imposed by the cold (previously BM now HAZ) supporting material. This refined grain structure will then be used as support for the

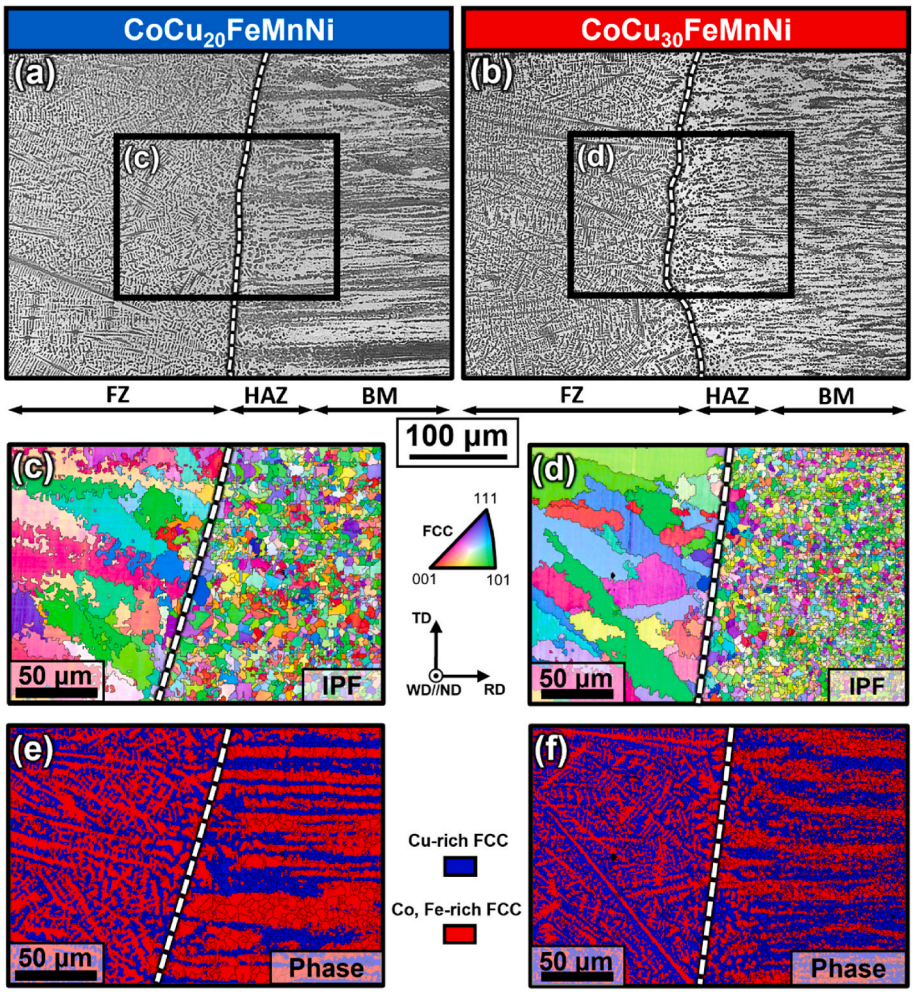

Fig. 4. Microstructural analysis at the fusion boundary, highlighting the optical microscopy image of the (a) $CoCu_{20}FeMnNi$ HEA and (b) $CoCu_{30}FeMnNi$ HEA and corresponding EBSD IPF and phase maps in (c) and (e) for the $CoCu_{20}FeMnNi$, and phase maps in (d) and (f) for the $CoCu_{30}FeMnNi$ HEA.

development of the large columnar grains observed in the FZ. Furthermore, observing the microstructure at the FZ centerline it is also possible to highlight that the variation in Cu content effectively caused different microstructural features to develop upon solidification of the molten pool, although the same welding conditions were used for both materials. In other terms, the synergistic influence of different thermophysical properties and composition coupled with different solidification paths will render different microstructures between the joints.

The highly oriented and columnar grains that developed during GTAW will introduce anisotropy on the mechanical properties in the FZ. This fact, combined with the existence of a highly deformed microstructure in the BM and of a small equiaxed grain structure in the HAZ, compounded by the columnar grains in the FZ, render the expectation of an inhomogeneous mechanical behavior across the joint.

Fig. 2 showcases the initial condition of the two BM prior to welding. It can be observed that in both cases the microstructure is comprised by interlayered elongated stripes corresponding to two different FCC phases (as seen by in EBSD phase maps in Fig. 2 a) and b)). Further characterization using EDS allows to characterize the phase's composition, as detailed in Fig. 2 c) to d). The elemental mapping data reveals that one of the FCC phases in both materials is rich in both Co and Fe, while the other FCC is primarily Cu- and Mn-rich. For this reason, from this point we address these two FCC phases as the Co, Fe-rich phase and the Cu-rich phase. It is also possible to observe that the $CoCu_{30}FeMnNi$ has a higher amount of the Cu-rich phase within it, which is related to its higher nominal content of Cu. Such is also highlighted in Table 1, where EDS point analysis results marked in Fig. 2 a) and b) are showcased.

As the phase distribution on both BMs is highly dependent on the processing conditions prior to welding, the associated phase diagrams depicted in Fig. 3 allow to infer on the possible phases passible to occur in the alloys during their thermomechanical processing. In both cases, at high temperatures liquid first solidifies into a FCC phase (FCC #1). Eventually, at ≈930 °C a different FCC phase (FCC #2) starts to form as part of a solid state transformation, as Cu and Mn diffuse into the FCC #1 grain boundaries, thus giving origin to the two mentioned major phases that were previously shown in Fig. 2 a) and b). Beyond these two phases, of relevant notice is also the formation of a B2 BCC phase, which is formed at ≈560 °C, for both alloy compositions. This cooling path is compliant with that found in the literature [8,20,21]. As such, it is important to highlight that the formation of the different FCC phases occurs in the solid state through solute diffusion.

Nevertheless, although phase diagrams can yield a basic understanding of the solidification of an alloy, these only consider equilibrium conditions with infinitively fast diffusion in both the liquid and the solid phases. Such is seldom achieved in real life processing conditions, especially during any fusion-based welding process, providing in this way sufficient conditions for other (metastable) phases to occur in the weld microstructure. However, in a first instance it allows us to infer upon the possible phases that may form upon the solidification of these HEAs. Further analysis is made through Scheil-Gulliver calculations, detailed further ahead in this paper, when analyzing the FZ microstructure evolution (in Fig. 5).

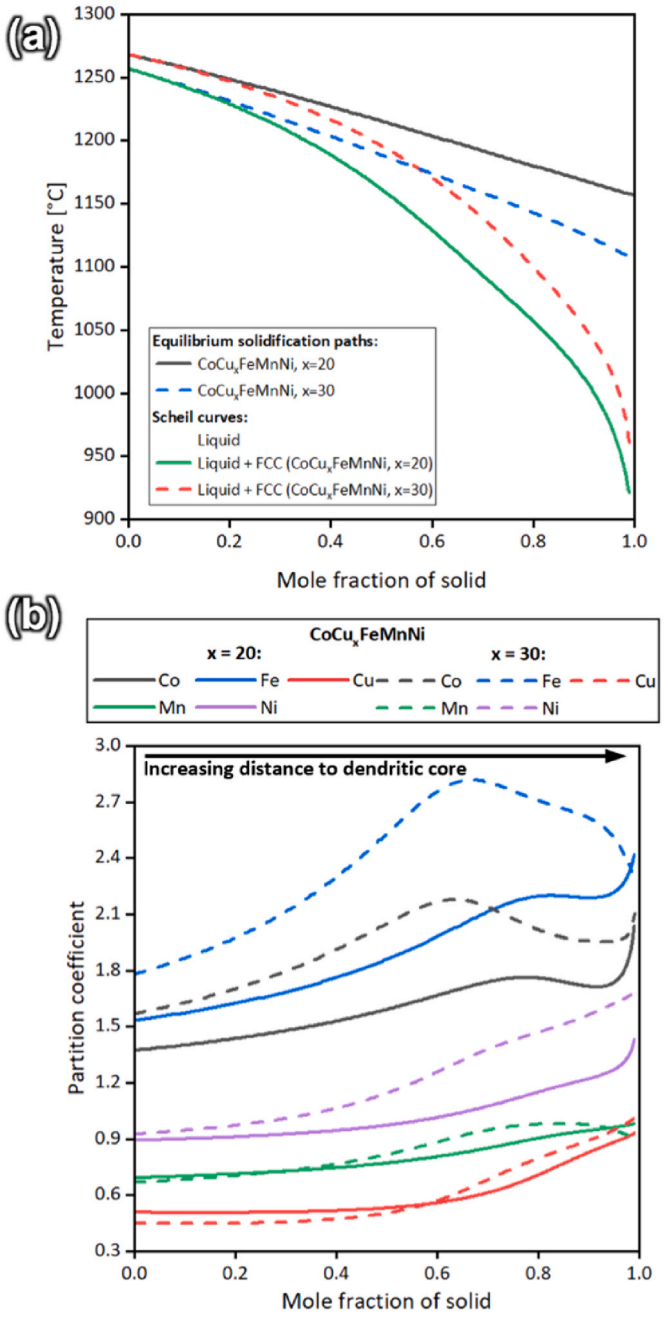

Fig. 5. (a) Simulation of the non-equilibrium solidification using Scheil-Gulliver method, and (b) partition coefficient of the elements throughout solidification.

Attention is now devoted to the fusion boundary (FB), and the regions surrounding it: the HAZ and FZ. From the HAZ we can observe that the microstructure is characterized by near equiaxed grains within elongated packs of the domains that contain the two FCC phases. From this, we can also observe grain growth phenomena that caused larger grains to develop with increasing size, when approaching the FZ. Such is particularly visible in Fig. 4(c) and (d).

The columnar dendritic nature of the FZ contrasting with the grains beyond the FB towards the BM can also be identified here, comprising also both FCC phases. We can qualitatively observe in the EBSD phase maps (refer to Fig. 4 e) and f)) that the $CoCu_{30}FeMnNi$ alloy comprises more of the Cu-rich FCC phase than the $CoCu_{20}FeMnNi$ in the corresponding FZ. Additionally, by complementing the IPF maps of Figs. 1 and 4 we can see that the grain size exhibited by this region is larger than any of the other regions of the weld, given the competitive growth phenomena that occurs during welding. This occurs as the grains present in the region that will comprise the HAZ, acts as a platform for new grains to grow in the maximum temperature gradient, which is aligned perpendicularly to the FZ centerline. As these new grains form, competitive growth takes place, where those which have their growth direction aligned with the easy growth direction (<001> for FCC materials) tend to grow faster and larger than those that are aligned in other directions. Such tendency can be seen in the IPF maps of Fig. 1, where the most grains in the FZ have a red color tone, corresponding to a predominant <001> orientation.

Furthermore, given the already mentioned non-equilibrium solidification conditions to which the molten pool is exposed to during welding (on both types of materials), the solidification paths can deviate from those calculated considering only equilibrium conditions. As such, to evaluate the microstructure under non-equilibrium conditions Fig. 5 a) displays the solidification curves of both alloys using the Scheil-Gulliver methodology available.

The solidification path details that for the $CoCu_{20}FeMnNi$ alloy, the liquid phase starts to solidify at ≈1270 °C, with a solidification range of ≈310 °C. Additionally, for the $CoCu_{20}FeMnNi$ case solidification starts at ≈1250 °C, ending at ≈910 °C, corresponding to a solidification range of ≈340 °C. Thus, it can be inferred that the addition of Cu in the material is beneficial to lower the solidification temperature range, which is often associated to hot cracking during welding. In both cases, the solidification curves only indicate the formation of a Co, Fe-rich FCC phase. A possible reason for the non-existence of the Cu-rich phase can be due to the fact that the Scheil model only assumes infinitively fast diffusion in the liquid, while neglecting the diffusion phenomena occurring in the solid phases. Nevertheless, according to the phase diagram, the Cu-rich FCC phase only forms at lower temperatures, after the liquid was fully consumed. This would be expected as the Scheil-Gulliver simulation does not consider diffusion on the solid state, which is the cause for the formation of a second FCC phase. To further detail the evolution upon solidification, we now turn to identify how elemental segregation occurs along the predicted solidification paths, considering the partition coefficient of all elements in the Co, Fe-rich phase during solidification, not considering solid-state transformations. These results are displayed in Fig. 5 b).

The partition coefficient can be calculated by dividing the concentration of an element on a solid phase and the concentration on the liquid. In this sense, if the partition coefficient attains values superior to 1, this means that such solid-state phase is being enriched by these elements. Should the partition coefficient reach values lower than 1, this indicates that such element is being segregated into the interdendritic liquid. Given this, the partition coefficient can help us to understand how the elements tend to be distributed within a forming dendrite. That is, the mole fraction of solid values that are closer to zero, correspond to when the liquid is starting to solidify, having a wide amount of all elements available for the formation of any solid phases. Such corresponds to the dendritic cores, which are the first regions to solidify. Contrarily, when the mole fraction of solid reaches values closer to 1, it means that the elements that are still available within the liquid eventually solidify at the interdendritic regions.

Considering the $CoCu_{20}FeMnNi$ case, it is possible to observe that the Fe and Co elements partition coefficient curves have a similar behavior, where it is possible to see that up to an approximately 0.80 mol fraction of solid, these tend to increase, meaning that the initially formed phase is being enriched by these elements. From that point on, their partition coefficient tends to decrease, indicating that the regions further away from the dendritic cores are getting depleted of these elements. However, when the mole fraction of solid is above 95 %, a sharp increase in the partition coefficient of Co, Fe and Ni can be observed. Particularly, in the case of Ni, the partition coefficient starts below 1 and exhibits an increasing tendency throughout all solidification path, meaning that the newly formed dendrites are getting enriched with this element. Finally,

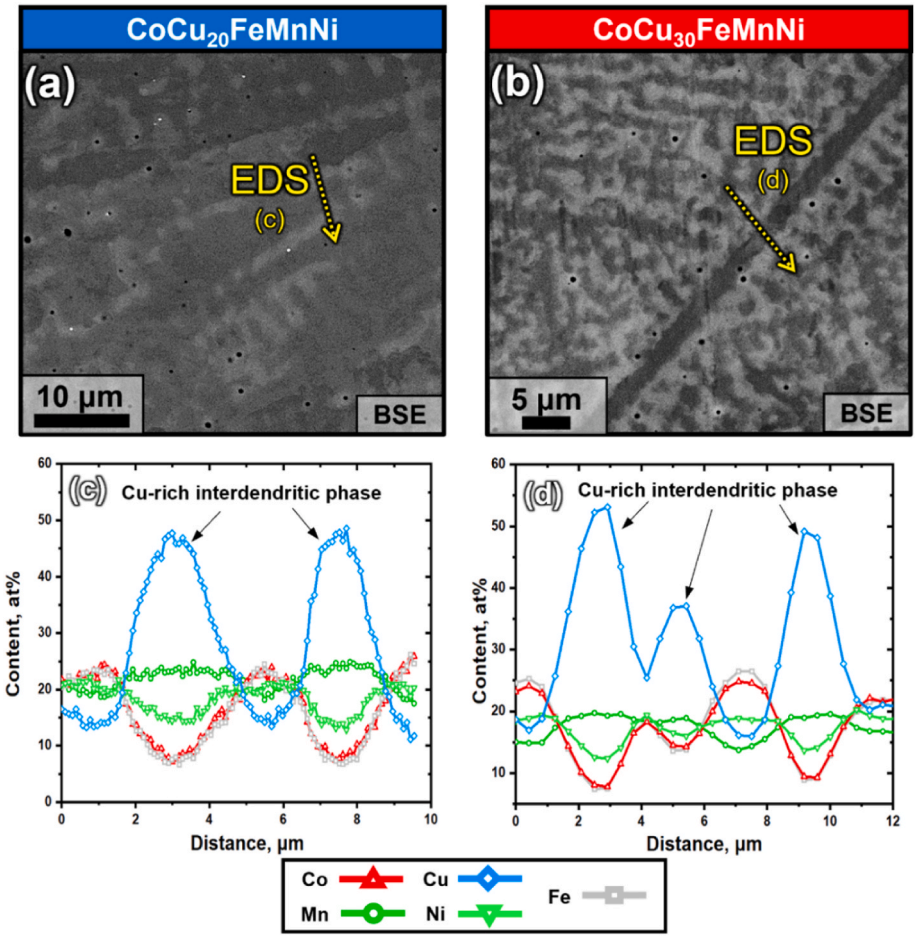

Fig. 6. Microstructural analysis of the fusion zone on the (a) $CoCu_{20}FeMnNi$ and (b) $CoCu_{30}FeMnNi$ HEAs in the as-welded condition, and corresponding EDS line scans (c) and (d).

the partition coefficient of Co and Mn is also consistently increasing. This indicates that we can expect a Cu and Mn concentration peak at the dendritic interfaces, as these elements are consistently being segregated into the liquid.

A similar behavior can be seen in the $CoCu_{30}FeMnNi$ case. However, here the Fe and Co peak occurs at an earlier stage, when the mole fraction of solid reaches a value of nearly 0.65. In this case elemental segregation is even more obvious, as the dendritic regions away from the core become depleted of these elements.

With this information it can be concluded that the dendritic cores are richer in Fe, Co and Ni, while the dendritic boundaries tend to be richer in Cu and Mn upon solidification. As such, it is possible to conclude that with further cooling, the formation of the Cu-rich FCC phase at the dendritic grain boundaries is eminent and very likely to occur, but as a solid state transformation. These thermodynamic-derived results agree with the EDS data obtained in the FZ of both welds displayed in Fig. 6. In fact, the element distribution results show coherence with the predicted compositional distribution obtained considering the partition coefficient, especially in the Co, Fe-rich phase and the Cu-rich phase, which also has Mn in a lower percentage in its constitution. However, it would have been expected a higher amount of Ni in the interdendritic region, which is not the case for both alloys' welded joints, as the EDS indicates that the Co, Fe-rich phase has more Ni than the Cu-rich phase. Such can be explained by the fact that no diffusion in the solid phase was considered for these non-equilibrium thermodynamic calculations. Additionally, the assimilation of Ni in the Co, Fe-rich dendrites can also occur in later stages of temperature decrease, as the Cu-rich phase starts to form.

3.2. Synchrotron X-ray diffraction of the welded joints

The phases present in the welded joints are further unveiled by the SXRD patterns displayed in Fig. 7 a), b), and c) corresponding to the BM, HAZ, and FZ, respectively. Such allows us to inspect on the potential formation of other phases in the material, that otherwise cannot be identified by either conventional or advanced microscopy (due to limited surfaces areas for analysis available, whereas high energy synchrotron radiation allows to work in transmission mode over wider regions, yielding improved statistics).

Starting from the BM, as expected it is possible to identify the two phases sharing the same FCC crystal structure and similar lattice parameters. Furthermore, analysis of the patterns corresponding to the HAZ reveals significant changes. Phase identification in this region allows to observe precipitation of a B2 BCC phase (at a lower intensity level) in the region of the joint for both alloys. Such a phase is predicted by one axis equilibrium diagrams (refer to Fig. 3) to nucleate at relative lower temperatures than the Cu-rich FCC (B2 BCC nucleates at ≈560 °C), which highlights the different thermal processing conditions that arose from the exposure of the solid-state material to the high temperatures impending from the molten pool. Nevertheless, in the FZ no indication of the formation of this B2 BCC was encountered in the patterns, only the two main FCC phases were encountered. This is coherent with the results obtained from the EBSD data and CalPhaD simulations.

The lattice parameters of these phases were determined from the diffraction patterns using Rietveld refinement (via GSAS II) and are depicted in Table 2. Here, the BM results show proximity to the HAZ and FZ, although with slight deviations which is to be expected given the

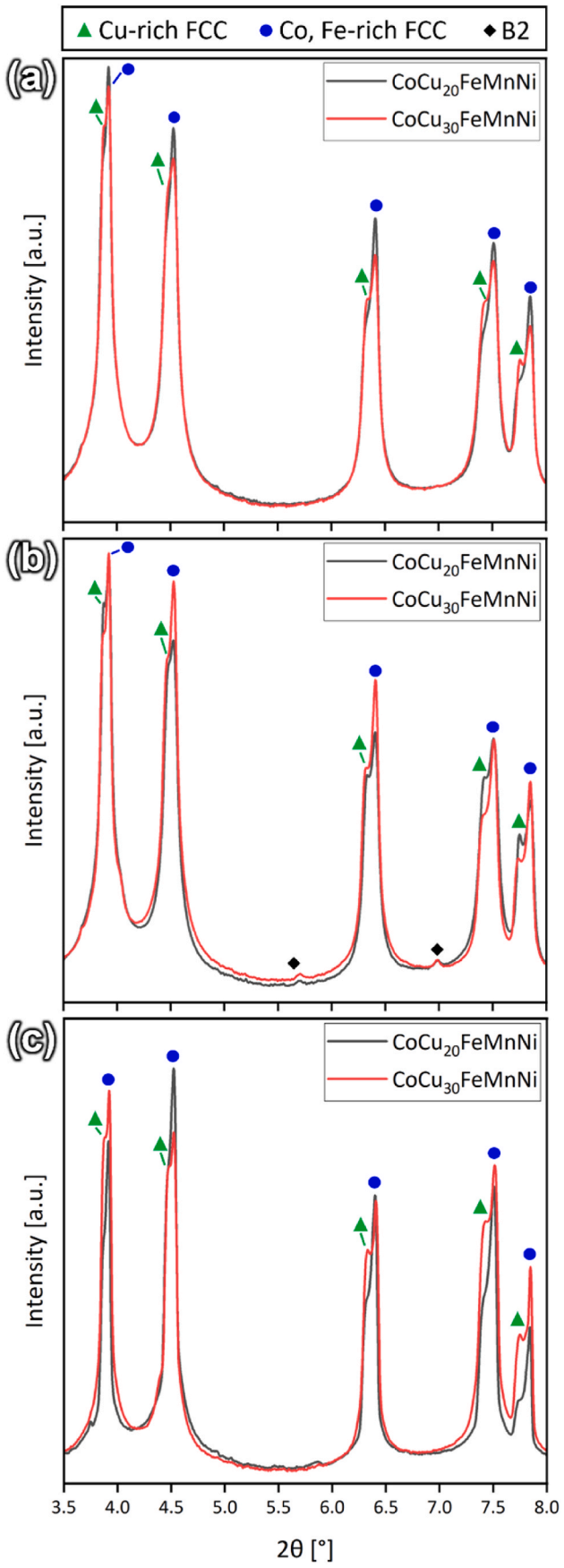

Fig. 7. Representative synchrotron X-ray diffraction patterns, from both HEAs welded joints on the: (a) BM, (b) HAZ, and (c) FZ.

Table 2
Lattice parameter in the HAZ and FZ (rounded to the fourth decimal case).

	Phase	Crystal structure (space group)	$CoCu_{20}FeMnNi$ [Å]	$CoCu_{30}FeMnNi$ [Å]
BM	**Co, Fe-rich FCC**	FCC (F m −3 m)	3.6008	3.6025
	Cu-rich FCC	FCC (F m −3 m)	3.6430	3.6442
HAZ	**Co, Fe-rich FCC**	FCC (F m −3 m)	3.6007	3.6013
	Cu-rich FCC	FCC (F m −3 m)	3.6403	3.6478
	B2 BCC	B2 BCC (P m 3 m)	2.8658	2.8599
FZ	**Co, Fe-rich FCC**	FCC (F m −3 m)	3.6031	3.6099
	Cu-rich FCC	FCC (F m −3 m)	3.6461	3.6466

different microstructure exhibited in each of these regions.

Further analysis of the synchrotron diffraction data reveals the phase volume fraction present in the base material of each alloy: the $CoCu_{20}$-FeMnNi BM is composed of 68.3 % of the Co, Fe-rich phase, while the remaining is Cu-rich FCC; for the $CoCu_{30}FeMnNi$ the fractions change to 62.8 % for the Co, Fe-rich phase, and 37.2 % of the Cu-rich phase. The phase fraction data obtained for the diffraction experiments is in good agreement with the EBSD phase maps, as previously shown in Fig. 2. Additionally, these results are also in accordance with the thermodynamical data shown in Figs. 3 and 5 b), since the Cu-rich phase nucleates at lower temperatures (thus being in a lower fraction), while Cu tends to migrate towards grain boundaries upon solidification in both HEAs.

Given the microstructure alterations occurring in the HAZ and FZ on both alloys, the phase volume fraction of each phase is also bound to differ from the BM. As such, starting on the HAZ of the $CoCu_{20}FeMnNi$ HEA, the results indicate that the phase volume fractions of each of the phases is 61.2, 34.1 and 4.7 % for the Co, Fe-rich, Cu-rich and B2 BCC phases, respectively. For the $CoCu_{30}FeMnNi$ HEA, however, the phase volume fraction distribution is 58.2, 39.5 and 2.3 % corresponding to the Co, Fe-rich FCC, Cu-rich FCC and B2 BCC.

Furthermore, the FZ is the region, where there is a more notorious modification in the phase fractions between both alloys. Here, the $CoCu_{20}FeMnNi$ HEA exhibits an overall amount of 78.9 % of the Co, Fe-rich phase (with the remaining 21.1 % corresponding to the Cu-rich phase), while the $CoCu_{30}FeMnNi$ HEA has a 51.1 and 48.9 % percentage of the Co, Fe-rich phase and Cu-rich phase, respectively. These phase volume fraction values contrast with those exhibited by the BM, which is mainly due to the different processing methods that each region of the weld was subjected to. Furthermore, the variation on phase volume fraction on the FZs of both joints can be related to the fact that the Cu-rich FCC nucleates at an earlier stage in the $CoCu_{30}FeMnNi$ HEA, thus yielding a larger amount of this phase on the corresponding FZ. Nevertheless, such phase volume fraction distribution may have a considerable influence on the final mechanical behavior of the resulting joints.

Nevertheless, before we delve into the mechanical properties of the welded joints, another important topic of discussion concerns the microstrain variation. The microstrain changes along the welds can be derived from the change in lattice parameters exhibited by each phase as obtained by SXRD. Such allows us to infer on the residual stress condition of the welds and role of the weld thermal cycle along the different regions of the joint. However, calculation of the microstrain requires knowledge of the unstrained interplanar spacing (d_0) of each of the phases in both materials. Using single-peak fitting, analysis was performed in the (311) diffraction peak of each of the FCC phases, and the (211) for the B2 BCC phase was also to retrieve the values for interplanar spacing (d) along the joints. The choice of these peaks for this analysis is based on their insensibility to intergranular strains in the FCC and BCC

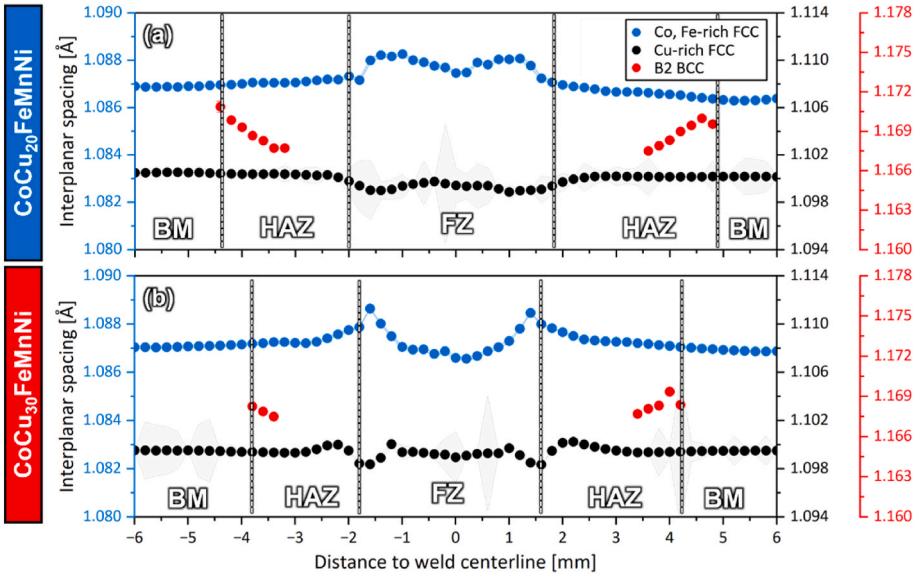

Fig. 8. Interplanar spacing distribution corresponding to the different phases identified throughout the microstructure of $CoCu_{20}FeMnNi$ (a) and $CoCu_{30}FeMnNi$ (b) welded HEAs.

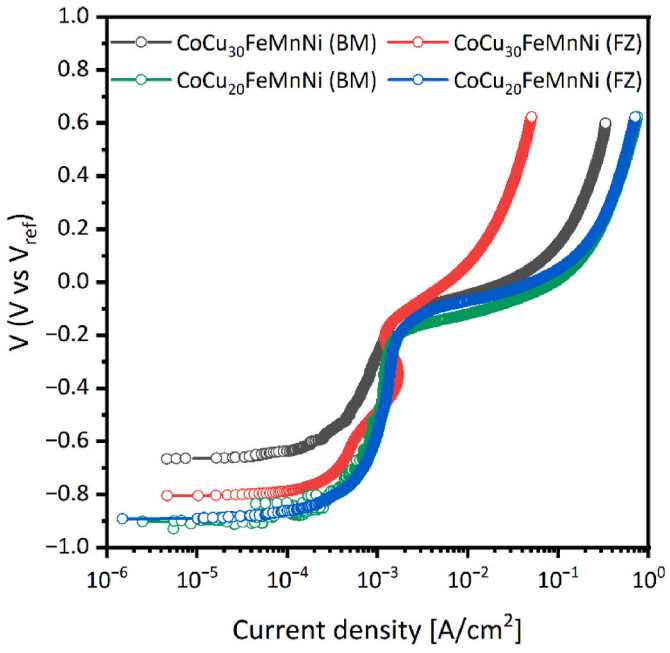

Fig. 9. Comparison between the polarization curves of the $CoCu_xFeMnNi$ (x = 20,30) BMs alongside with the corresponding FZs.

crystal structures, respectively [22]. The variation is depicted in Fig. 8.

In both cases, it is evidenced that the d values are constant in the BM, which was expected. Eventually, the presence of the B2 BCC phase marks the beginning of the HAZ, where the d-spacing for this phase tends to decrease. As the B2 BCC diffraction peaks disappear, the HAZ in both welds continues until reaching the fusion boundary, where an increase on the d-spacing can be observed in the Co, Fe-rich FCC phase. The disappearance of the B2 BCC phase is related to the temperature and time to which a given region of the weld was subject to. Being located in the region of the HAZ further away from the FZ (where the maximum temperatures are attained), the conditions for the nucleation of the B2 BCC phase are granted, given that this phase is characterized by its nucleation at relatively lower temperatures, as indicated in Fig. 3.

Furthermore, in the FZ a consequent decrease on the d-spacing of the Cu-rich phase can also be observed, such is related to the marked impact in the microstructure caused by the GTAW. This disparity in d-spacing values is especially visible in the $CoCu_{30}FeMnNi$ welded joint, where a not so smooth evolution translates the complex microstrain state of the joint at the fusion boundary. Nevertheless, eventually in the bulk of the FZ the d-spacing values evidence a decrease, achieving values closer to those exhibited by the BM.

3.3. *Electrochemical characterization of the joints*

To assess the corrosion behavior of the welded joints, the two extreme microstructural conditions of the joints, that is BM and FZ, were analyzed. As such, representative anodic polarization curves comparing the BM and FZ of both types of samples are displayed in Fig. 9. Using the Tafel model [23,24], the corresponding corrosion currents, I_{corr}, were extrapolated to be 24.8 μA/cm^2 for the $CoCu_{20}FeMnNi$ BM and 28.2 μA/cm^2 for the $CoCu_{30}FeMnNi$ BM. Considering the corresponding FZs, the extrapolated I_{corr} for the $CoCu_{20}FeMnNi$ case was 94.9 μA/cm^2, while for the $CoCu_{30}FeMnNi$ joint the value was 153.3 μA/cm^2. Such allows us to verify that deterioration of the corrosion behavior can be seen in both cases when comparing the BMs to their corresponding FZs, being more prominent in the $CoCu_{30}FeMnNi$ HEA case.

On the other hand, comparison of the corrosion potential, E_{corr}, for each condition, revels that for the $CoCu_{20}FeMnNi$ case, the BM and the FZ showcase values of −0.891 V and −0.894V, respectively. These however, contrast with those extrapolated in from the $CoCu_{30}FeMnNi$ joint, where the BM, corresponding to −0.667 V, exhibits a significantly higher value than its corresponding FZ (−0.806 V). This indicates that the $CoCu_{30}FeMnNi$ HEA has a lower tendency to corrode than the other analyzed regions.

Likewise, the EIS measurements, performed the BM and the FZ of both samples are presented in Fig. 10, in terms Bode and Nyquist diagrams. There it is possible to observe that, at low frequencies, the impedance modulus, |Z|, of the BMs reach values up to 50.3 Ω for the $CoCu_{20}FeMnNi$ HEA and 528.4 Ω for the $CoCu_{30}FeMnNi$ HEA. Conversely, for each analyzed FZ the maximum measured values were 63 Ω and 141 Ω, respectively. Additionally, the maximum values attained for the phase angle was ≈-0.27° for the $CoCu_{20}FeMnNi$ BM and ≈-0.7° in the $CoCu_{30}FeMnNi$ BM case. Similar values were noted for the $CoCu_{20}FeMnNi$ FZ, corresponding to ≈ -0.35°, while in the

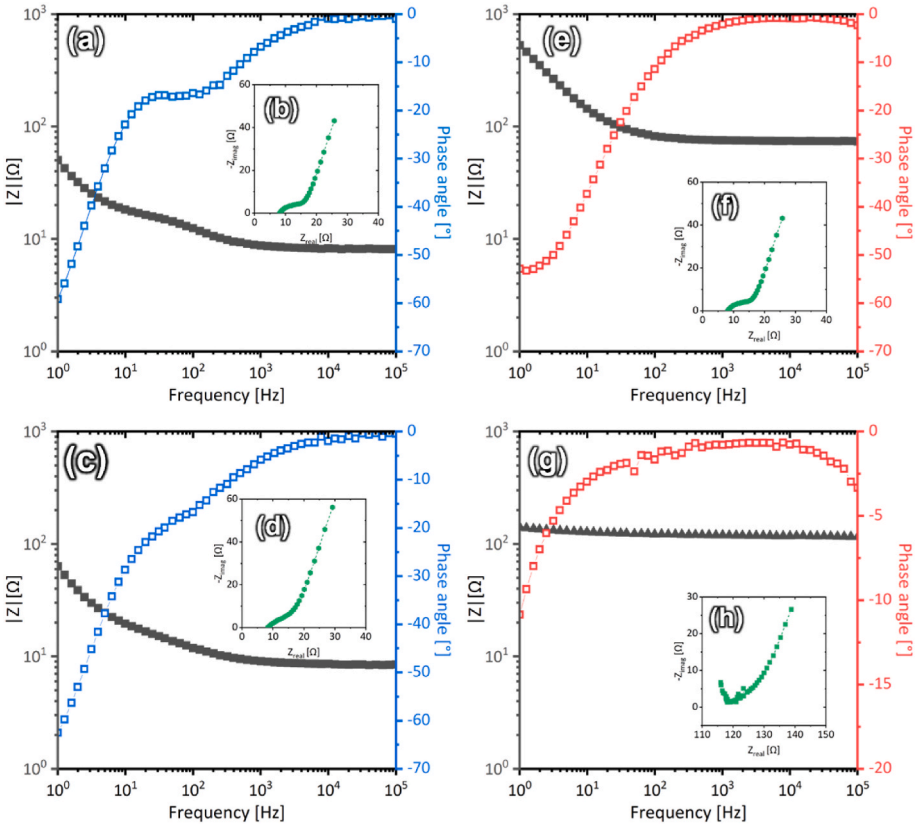

Fig. 10. EIS measurements of the welded joints: (a) and (b) are the Bode and Nyquist diagrams of the $CoCu_{20}FeMnNi$ BM, respectively, while (c) and (d) are the Bode and Nyquist diagrams of its corresponding FZ; (e) and (f) correspond to the Bode and Nyquist diagrams of the $CoCu_{30}FeMnNi$ BM and (g) and (h) are the Bode and Nyquist diagrams of the $CoCu_{30}FeMnNi$ FZ.

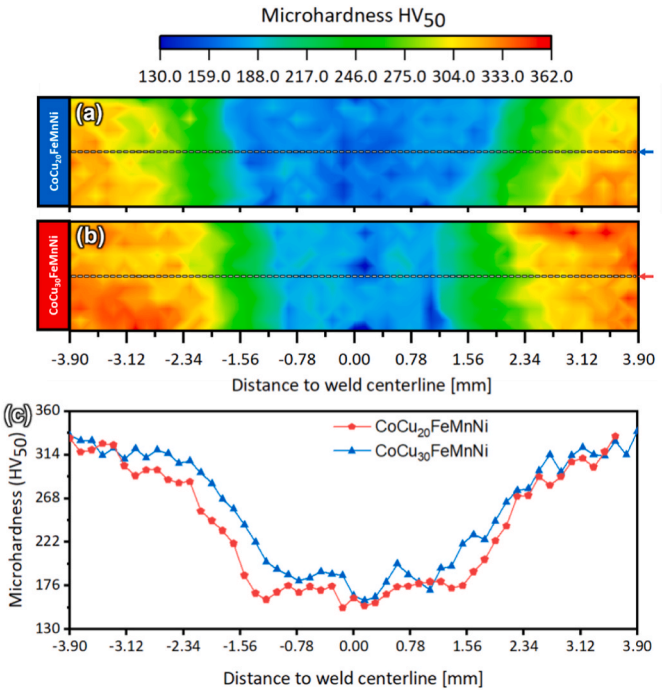

Fig. 11. Microhardness distribution along the (a) $CoCu_{20}FeMnNi$ and (b) $CoCu_{30}FeMnNi$ welded HEAs. Comparison of the hardness variation taken from the middle line of the map is displayed in (c).

$CoCu_{30}FeMnNi$ FZ a distinct behavior from its corresponding BM was verified, these measured to be ≈ -0.66°.

Overall, these values agree with those expected from the polarization curves, where the corrosion behavior of the $CoCu_{30}FeMnNi$ FZ is significantly more different than its corresponding BM, which in the $CoCu_{20}FeMnNi$ joint is not as obvious. From this we can infer that the microstructure in terms of the synergistic effect of dislocation density, phase fraction and composition in each welded region, are prone to be important factors to the optimization of the electrochemical properties of the joints on both HEAs.

3.4. Mechanical properties assessment via microhardness mapping and tensile testing

Considering the evolution of microstructure and the microstrain distribution previously unveiled, it is important to evaluate the mechanical performance of the welded joints to assess their potential use as part of structural components. This is the premise on which the inspection of such novel metals using welding technologies is based on. Fig. 11 displays the microhardness distribution along each welded joint. A major difference between samples is the extension of each weld, where the FZ of the $CoCu_{20}FeMnNi$ is larger than that of the $CoCu_{30}FeMnNi$ HEA (≈2.7 mm vs ≈ 2.55 mm). This can be explained by the different thermal dissipation conditions granted by each phase upon their nucleation on the welded joints, clearly suggesting that the thermal field experienced by this portion of the welded joints is different.

As such, thermal conductivity calculations per phase were performed based on the nominal compositions of both alloys. The results evidence that upon its nucleation and subsequent phase transformations, the Co, Fe-rich FCC phase holds an approximately constant thermal conductivity value of 23 W/mK. The same, however, is not the case of the Cu-

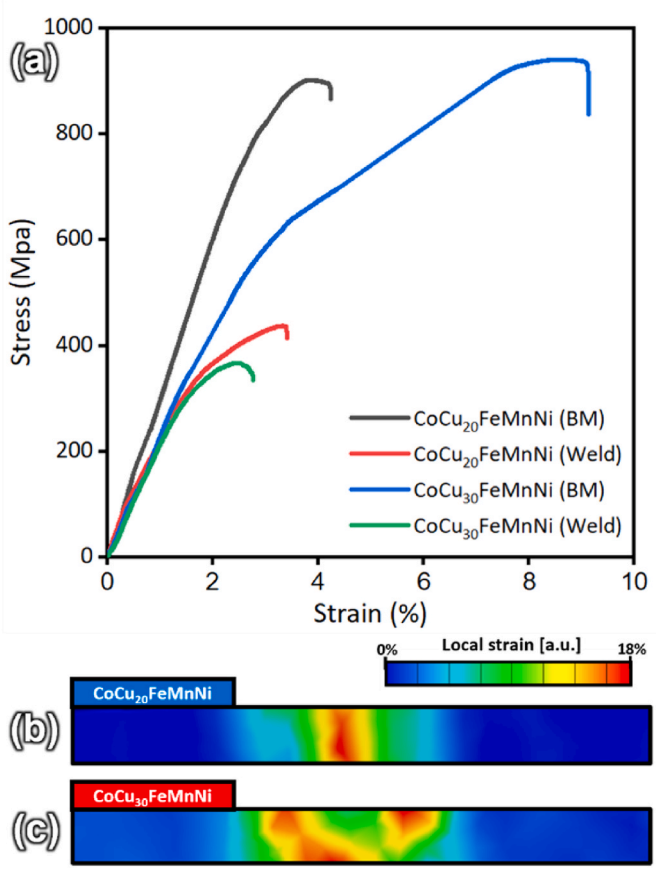

Fig. 12. (a) Representative stress-strain curves obtained from both HEAs in the as-welded and base material conditions. Digital image correlation images taken prior to fracture of the (b) $CoCu_{20}FeMnNi$ and (c) $CoCu_{30}FeMnNi$ welded HEAs, highlighting the FZ as the softest and weakest point of the joint.

rich FCC, where the thermal conductivity increases from ≈54 W/mK (upon its nucleation) to ≈ 100 W/mK (at 500 °C), in the $CoCu_{20}FeMnNi$ case. For the $CoCu_{30}FeMnNi$ HEA, as the Cu-rich FCC begins to nucleate at a an earlier stage (refer to Fig. 3), its thermal conductivity goes from ≈27 W/mK reaching ≈ 100 W/mK at 500 °C). This allows us to infer that heat dissipation conditions were different between welded samples, although the same welding parameters were utilized, thus resulting in different dimensions for the HAZ and FZ. This is also coherent with the larger extent of the region containing the B2 BCC phase on the $CoCu_{20}FeMnNi$ material, highlighting that heat transfer was more efficient in the $CoCu_{30}FeMnNi$ case, by not providing sufficient time for more B2 BCC to form (as it would be expected from the one-axis equilibrium diagram in Fig. 3).

Overall, the microhardness distribution in both types of samples is similar. The results reached a maximum of ≈361 HV_{50} in the BM and a minimum of ≈137 HV_{50} in the FZ. Such decrement in the microhardness of the FZ can be related with the large grain size characteristic of this region visible in Fig. 1.

Further analysis of the mechanical properties was done by performing tensile tests. Representative stress-strain curves of both BMs and corresponding welded joints are displayed in Fig. 12 a). As it is possible to observe from the tensile behavior of both BMs, the $CoCu_{30}FeMnNi$ HEA reached a higher elongation than the $CoCu_{20}FeMnNi$ HEA, with corresponding values of 9.1 and 4.2 %, respectively. Considering the ultimate tensile strength (UTS), the $CoCu_{20}FeMnNi$ BM possesses a slightly lower strength than the $CoCu_{30}FeMnNi$ HEA: 902 vs 942 MPa, respectively. These results indicate that the Cu enrichment on the composition positively contributes to its mechanical performance. This occurs as the increase of Cu as alloying element on the composition of the $CoCu_{30}FeMnNi$ HEA, contributes to an enhancement in its ductility, allowing it to become more ductile as the fraction of Cu-rich phase also increases. The higher amount of this ductile phase, combined with the remaining Cu confined in the Fe, Co-rich FCC, then translates into the increase in ductility on the HEA.

Considering the resulting welded joints, however, it can be observed that the tensile properties of both materials deteriorated considerably, with the Cu-lean HEA possessing a strength of 437 MPa, while the Cu-rich reached 368 MPa. As for the elongation, the welded joints performed poorly compared to their BMs counterparts. However, the drop in elongation was more significant for the $CoCu_{30}FeMnNi$ case (8.6 vs 2.5 %), rather than the Cu-lean alloy (3.8 vs 3.3 %). This decrement in both strength and elongation primarily stems from the microstructure changes induced by the weld thermal cycle. In fact, the gradient of microstructures that are found in both joints (deformed grains in the BM, small equiaxed grains in the HAZ and predominantly large columnar grains in the FZ), will render not only an heterogenous deformation behavior. In fact, strain will tend to be concentrated in the low hardness FZ, which is further compounded by the anisotropic behavior arising from the columnar grain structure present at this region of the joint.

Such factors are further intensified by the microstrain distribution in the $CoCu_{30}FeMnNi$ welded joint (refer to Fig. 8). Here it is possible to infer that the local strain concentration is higher near the fusion boundary than in the bulk of the FZ. The same does not occur in the Cu-lean weld, where a smooth microstrain transition from the BM to the FZ can be observed. Additionally, the phase fraction ratio between the major FCC phases can also be detrimental to the mechanical performance of the welds, as the higher content of the Cu-rich FCC can be detrimental to the maximum strength achieved by the alloy, although granting it more ductility, when a homogenous microstructure distribution can be found (as in the case of the BMs).

Nevertheless, evidence of the relatively poor mechanical performance of the welded joints can be found in Fig. 12 b) and c), taken prior to fracture during tensile testing. Here it is possible to observe that the fusion zone, being the softest region in both materials, is also the location, where most of the strain is sustained, leading to fracture in this region in both cases. These results are coherent with the impact that the microstrain levels encountered in the welds (refer to Fig. 8) on the local strain distribution, which is observed via DIC. Given this, it is possible to observe that the mentioned sharper increase of d-spacing at the fusion boundary on the $CoCu_{30}FeMnNi$ weld results on the fracture on this region, instead of the center of the FZ, which is the case of the Cu-lean welded joint.

The fracture surfaces of the joints are shown in Fig. 13. In both cases there is evidence of interdendritic cracking, occurring as brittle type of failure. Such is caused by the inhomogeneous phase distribution on the FZ, alongside their compositional differences. This results in the previously mentioned anisotropy of mechanical properties on the different regions within the material, which can then generate stress concentration in between the interdendritic boundaries, making them susceptible to cracking. With progression of the tensile test, small sized fractures are formed amongst the large dendritic grains. As these fractures coalesce, the inevitable failure of the joints occurs, leaving behind dendritic markings on the surface.

4. Conclusions

The present study highlighted the differences in microstructure and mechanical performance arising from the gas tungsten arc welding on a $CoCu_xFeMnNi$ (x = 20,30) HEAs. The results showed that although defect-free joints could be achieved, the mechanical performance was diminished. The main reason being the inhomogeneous microstructure achieved throughout the weld.

Furthermore, in terms of microstructure, multiple characterization methods allowed to observe the phase distribution of both welded HEAs, comprised by two different major FCC phases. Of special notion, high

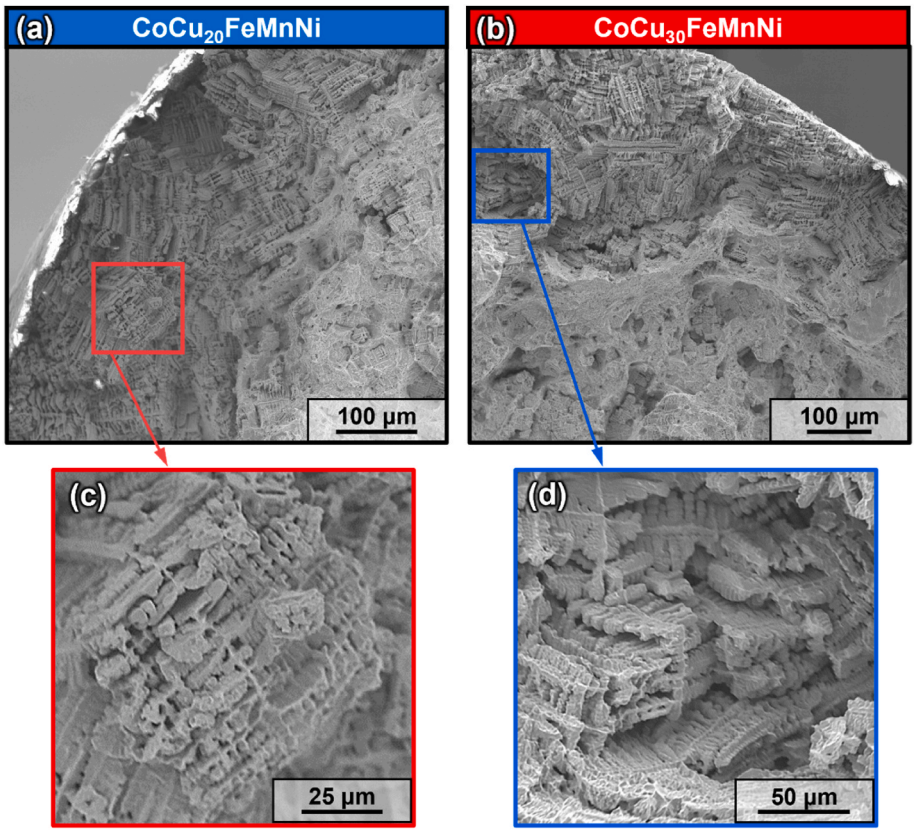

Fig. 13. Fracture surfaces of welded specimens: (a) $CoCu_{20}FeMnNi$ and (b) $CoCu_{30}FeMnNi$ welded joints and corresponding detailed views in (c) and (d), respectively.

energy synchrotron X-ray diffraction permitted to observe that the major differences between the welded samples resided on the phase fraction distribution developed upon welding. Through this technique, it was possible to identify a B2 BCC phase in the HAZ, which is predicted by thermodynamic calculations.

Additionally, electrochemical characterization of the joint revealed that upon welding the corrosion properties of each FZ are deteriorated. This effect was more evident in the $CoCu_{30}FeMnNi$ material. However, further analysis of the corrosion behavior of the joints envisages a comprehensive analysis of the interplay between the various microstructural features (including dislocations and phase composition) and their distribution on each region of the weld.

Moreover, the welded joints mechanical performance is significantly lower than those of the original BM, with the $CoCu_{30}FeMnNi$ case being the one that exhibited a higher contrast in the maximum strength and ductility achieved during tensile testing. Such is a product of the different microstructures across the joint combined with the microstrain developed throughout the welds upon the non-equilibrium solidification of the molten pool. These can facilitate crack initiation upon mechanical solicitation, especially when large grains of two dissimilar phases, with very different compositions, are present in the microstructure.

As such, future work should envisage the use of post-weld heat treatment to modify and improve the microstructure and mechanical properties of these welded joints. The grain size disparity between the BM and the FZ is also of major concern, as achieving a FZ comprising refined grains can play an important role in improving the mechanical performance of the welded HEAs. Taking this into consideration, research on how the phases present within the microstructure interact with each other during loading is also a relevant topic, as it can supply the grounds to further improve these HEAs concerning their weldability and consequent mechanical performance.

CRediT authorship contribution statement

J.G. Lopes: Writing – review & editing, Writing – original draft, Visualization, Methodology, Investigation, Formal analysis, Data curation, Conceptualization. **M. Varela:** Methodology, Investigation, Data curation. **S.H. Shim:** Methodology, Investigation, Formal analysis, Data curation. **N. Schell:** Resources, Investigation. **E. Maawad:** Resources, Investigation. **S.I. Hong:** Resources, Investigation. **A.C. Baptista:** Resources, Investigation, Data curation. **J.P. Oliveira:** Writing – review & editing, Writing – original draft, Visualization, Validation, Supervision, Resources, Investigation.

Declaration of competing interest

The authors declare that they have no known competing financial interests or personal relationships that could have appeared to influence the work reported in this paper.

Data availability

Data will be made available on request.

Acknowledgements

JGL and MV acknowledge Fundação para a Ciência e a Tecnologia (FCT - MCTES) for its financial support via the project UID/00667/2020 (UNIDEMI). JGL acknowledges Fundação para a Ciência e a Tecnologia (FCT - MCTES) for funding the Ph.D. Grant 2020.07350.BD. JPO and ACB acknowledge the funding by national funds from FCT - Fundação para a Ciência e a Tecnologia, I.P., in the scope of the projects LA/P/0037/2020, UIDP/50025/2020 and UIDB/50025/2020 of the Associate Laboratory Institute of Nanostructures, Nanomodelling and

Nanofabrication – i3N. The authors acknowledge DESY (Hamburg, Germany), a member of the Helmholtz Association HGF, for the provision of experimental facilities. Beamtime was allocated for the proposal I-20211528 EC. The research leading to this result has been supported by the project CALIPSOplus under the Grant Agreement 730872 from the EU Framework Programme for Research and Innovation HORIZON 2020.

References

[1] B. Cantor, I.T.H. Chang, P. Knight, A.J.B. Vincent, Microstructural development in equiatomic multicomponent alloys, Mater. Sci. Eng. 375–377 (2004) 213–218, https://doi.org/10.1016/j.msea.2003.10.257.

[2] J.W. Yeh, Recent progress in high-entropy alloys, Ann. Chimie Sci. Matériaux 31 (2006) 633–648, https://doi.org/10.3166/acsm.31.633-648.

[3] D.B. Miracle, O.N. Senkov, A critical review of high entropy alloys and related concepts, Acta Mater. 122 (2017) 448–511, https://doi.org/10.1016/j.actamat.2016.08.081.

[4] S. Gorsse, J.P. Couzinié, D.B. Miracle, From high-entropy alloys to complex concentrated alloys, C R Phys 19 (2018) 721–736, https://doi.org/10.1016/J.CRHY.2018.09.004.

[5] S. Kou, Welding Metallurgy, 2002, https://doi.org/10.1002/0471434027.

[6] J.G. Lopes, J.P. Oliveira, A short review on welding and joining of high entropy alloys, Metals 10 (2020), https://doi.org/10.3390/met10020212.

[7] J.G. Lopes, P. Agrawal, J. Shen, N. Schell, R.S. Mishra, J.P. Oliveira, Evolution of microstructure and mechanical properties in gas tungsten arc welded dual-phase Fe50Mn30Co10Cr10 high entropy alloy, Mater. Sci. Eng. 878 (2023) 145233, https://doi.org/10.1016/J.MSEA.2023.145233.

[8] R. Sonkusare, P. Divya Janani, N.P. Gurao, S. Sarkar, S. Sen, K.G. Pradeep, K. Biswas, K. Biswas, Phase equilibria in equiatomic CoCuFeMnNi high entropy alloy. https://doi.org/10.1016/j.matchemphys.2017.08.051, 2017.

[9] S. Hun Shim, H. Pouraliakbar, S. Ig Hong, High strength dual fcc phase CoCuFeMnNi high-entropy alloy wires with dislocation wall boundaries stabilized by phase boundaries. https://doi.org/10.1016/j.msea.2021.141875, 2021.

[10] Y. Bin Kang, S. Hoon Shim, K. Ho Lee, S. Ig Hong, Dislocation creep behavior of CoCrFeMnNi high entropy alloy at intermediate temperatures. https://doi.org/10.1080/21663831.2018.1543731, 2018.

[11] Y.-G. Tong, N. Tian, H. Chen, X.-C. Zhang, Y.-L. Hu, X.-X. Ji, M.-J. Zhang, C.-J. Zhao, Real-time atomic deformation behavior of nano CoCrCuFeNi high-entropy alloy, Trans. Nonferrous Metals Soc. China 33 (2023) 1156–1163, https://doi.org/10.1016/S1003-6326(23)66172-2.

[12] S. Hun Shim, S. Min Oh, J. Lee, S.-K. Hong, S. Ig Hong, Nanoscale modulated structures by balanced distribution of atoms and mechanical/structural stabilities in CoCuFeMnNi high entropy alloys. https://doi.org/10.1016/j.msea.2019.138120, 2019.

[13] Y. Keun Kim, B. Ju Lee, S.-K. Hong, S. Ig Hong, Strengthening and fracture of deformation-processed dual fcc-phase CoCrFeCuNi and CoCrFeCu 1.71 Ni high entropy alloys. https://doi.org/10.1016/j.msea.2020.139241, 2020.

[14] Y. Keun Kim, S. Hun Shim, B. Ju Lee, S. Ig Hong, Correlation between mechanical properties and thermodynamic parameters of dual-fcc-phase CoCrFeCu x Ni (x = 1, 1.71) and CoCu 1.71 FeMnNi, (n.d.). https://doi.org/10.1016/j.matlet.2020.127866.

[15] J. Fiocchi, R. Casati, A. Tuissi, C.A. Biffi, Laser beam welding of CoCuFeMnNi high entropy alloy: processing, microstructure, and mechanical properties, Adv. Eng. Mater. 24 (2022), https://doi.org/10.1002/ADEM.202200523.

[16] M.A. Karimi, M. Shamanian, M.H. Enayati, Microstructural and mechanical properties assessment of transient liquid phase bonding of CoCuFeMnNi high entropy alloy, Trans. Nonferrous Metals Soc. China 31 (2021) 3063–3074, https://doi.org/10.1016/S1003-6326(21)65715-1.

[17] C. Prescher, V.B. Prakapenka, DIOPTAS: a Program for Reduction of Two-Dimensional X-Ray Diffraction Data and Data Exploration, vol. 35, 2015, pp. 223–230, https://doi.org/10.1080/08957959.2015.1059835, 10.1080/08957959.2015.1059835.

[18] B.H. Toby, R.B. Von Dreele, GSAS-II: the Genesis of a Modern Open-Source All Purpose Crystallography Software Package, vol. 46, 2013, pp. 544–549, https://doi.org/10.1107/S0021889813003531. Urn:Issn:0021-8898.

[19] J.O. Andersson, T. Helander, L. Höglund, P. Shi, B. Sundman, Thermo-Calc & DICTRA, computational tools for materials science, Calphad 26 (2002) 273–312, https://doi.org/10.1016/S0364-5916(02)00037-8.

[20] B.E. Macdonald, Z. Fu, X. Wang, Z. Li, W. Chen, Y. Zhou, D. Raabe, J. Schoenung, H. Hahn, E.J. Lavernia, Influence of phase decomposition on mechanical behavior of an equiatomic CoCuFeMnNi high entropy alloy, Acta Mater. 181 (2019) 25–35, https://doi.org/10.1016/j.actamat.2019.09.030.

[21] S.H. Shim, H. Pouraliakbar, H. Minouei, M.S. Rizi, V. Fallah, Y.-S. Na, H. Han, S. I. Hong, Characterization of the microscale/nanoscale hierarchical microstructure of an as-cast CrMnFeNiCu high-entropy alloy with promising mechanical properties. https://doi.org/10.1016/j.jallcom.2023.170091, 2023.

[22] J. Shen, J.G. Lopes, Z. Zeng, Y.T. Choi, E. Maawad, N. Schell, H.S. Kim, R.S. Mishra, J.P. Oliveira, Deformation behavior and strengthening effects of an eutectic AlCoCrFeNi2.1 high entropy alloy probed by in-situ synchrotron X-ray diffraction and post-mortem EBSD, Mater. Sci. Eng. 872 (2023) 144946, https://doi.org/10.1016/J.MSEA.2023.144946.

[23] I. Barauskienė, G. Laukaitis, E. Valatka, Stainless steel as an electrocatalyst for overall water splitting under alkaline and neutral conditions, J. Electroanal. Chem. 950 (2023) 117880, https://doi.org/10.1016/J.JELECHEM.2023.117880.

[24] S. Singh, C. Srivastava, Effect of carbon nanotube incorporation on the evolution of morphology, phase and compositional homogeneity, surface oxide chemistry and corrosion behaviour of electrodeposited FeCuMnNiCo-carbon nanotube composite coatings, Electrochim. Acta 439 (2023) 141639, https://doi.org/10.1016/J.ELECTACTA.2022.141639.